NEUROIMAGING

Functional ultrasound imaging of human brain activity through an acoustically transparent cranial window

Claire Rabut[1]†, Sumner L. Norman[2]*†, Whitney S. Griggs[2]†, Jonathan J. Russin[3], Kay Jann[4], Vasileios Christopoulos[5], Charles Liu[2,3,6]*, Richard A. Andersen[2,7]*, Mikhail G. Shapiro[1,8,9]*

Visualization of human brain activity is crucial for understanding normal and aberrant brain function. Currently available neural activity recording methods are highly invasive, have low sensitivity, and cannot be conducted outside of an operating room. Functional ultrasound imaging (fUSI) is an emerging technique that offers sensitive, large-scale, high-resolution neural imaging; however, fUSI cannot be performed through the adult human skull. Here, we used a polymeric skull replacement material to create an acoustic window compatible with fUSI to monitor adult human brain activity in a single individual. Using an in vitro cerebrovascular phantom to mimic brain vasculature and an in vivo rodent cranial defect model, first, we evaluated the fUSI signal intensity and signal-to-noise ratio through polymethyl methacrylate (PMMA) cranial implants of different thicknesses or a titanium mesh implant. We found that rat brain neural activity could be recorded with high sensitivity through a PMMA implant using a dedicated fUSI pulse sequence. We then designed a custom ultrasound-transparent cranial window implant for an adult patient undergoing reconstructive skull surgery after traumatic brain injury. We showed that fUSI could record brain activity in an awake human outside of the operating room. In a video game "connect the dots" task, we demonstrated mapping and decoding of task-modulated cortical activity in this individual. In a guitar-strumming task, we mapped additional task-specific cortical responses. Our proof-of-principle study shows that fUSI can be used as a high-resolution (200 μm) functional imaging modality for measuring adult human brain activity through an acoustically transparent cranial window.

INTRODUCTION

Measuring brain function in adult humans is essential for the diagnosis, monitoring, treatment, and research of neurological and psychiatric disease. Current brain activity recording techniques have substantial trade-offs concerning sensitivity, coverage area, invasiveness, and participant mobility during imaging. Noninvasive methods like functional magnetic resonance imaging (fMRI) offer whole-brain access but suffer from limited sensitivity and spatiotemporal resolution and restrict participant movement during imaging. Scalp electroencephalography and functional near-infrared spectroscopy (fNIRS), although more portable, have variable signal quality and are unable to accurately measure deep brain function. Invasive techniques such as intracranial electroencephalogram and electrocorticography provide superior resolution but involve electrode insertion beneath the skull or into the brain, limiting their scalability and functional lifetime. Despite their benefits, such invasive techniques are predominantly limited to severely impaired participants because of the inherent risks involved. Ultrasound localization microscopy (ULM) offers below-10-μm super-resolution for brain vasculature imaging (*1*), yet its functional utility is constrained by the need for intravenous microbubble delivery and long data collection windows. Recent advancements such as functional ULM (*2*) recover temporal resolution by averaging multiple trials; however, real-time, single-trial functional ULM imaging remains impractical for most human studies and brain-machine interface applications. Thus, there is a distinct need for neurotechnologies that optimally balance the tradeoffs between invasiveness and performance.

Functional ultrasound imaging (fUSI) is an emerging neuroimaging technique that spans the gap between invasive and noninvasive methods. On the basis of power Doppler imaging, fUSI measures changes in cerebral blood volume within a several-centimeters field of view by detecting the backscattered echoes from moving red blood cells. These cerebral blood volume changes are correlated with single neuron activity and local field potentials via neurovascular coupling (*3*, *4*). The spatial precision of fUSI approaches 100 μm with a framerate of up to 10 Hz, allowing fUSI to detect the function of small populations of neurons (*5*). This imaging modality does not expose the individual to radiation, is portable, and has been proven across multiple animal models, including rodents, ferrets, birds, nonhuman primates, and humans (*6*, *7*).

Brain imaging by fUSI does not require the use of contrast agents or electrode implantation and the imaging equipment sits outside the brain's protective dura mater; however, fUSI does require removal of an area of skull in large animals whose skulls are too thick for ultrasound waves to penetrate effectively in high resolution imaging paradigms. Transmission frequencies for fUSI range from 5 to 18 MHz (*6*), leading to aberration and attenuation by skull bone (*8*). Less aberration and attenuation can be achieved with frequencies in the 500-kHz range, such as those used in transcranial focused ultrasound (*9*); however, lower frequencies result in lower spatial resolution (3 mm at 500 kHz) and less Doppler sensitivity (*10*), which would mean that the imaging would underperform compared with fMRI. With sensitivity greater than 10 times that of fMRI (*11*), fUSI

[1]Division of Chemistry and Chemical Engineering, California Institute of Technology, Pasadena, CA 91125, USA. [2]Division of Biology and Biological Engineering, California Institute of Technology, Pasadena, CA 91125, USA. [3]USC Neurorestoration Center and the Departments of Neurosurgery and Neurology, University of Southern California, Los Angeles, CA 90033, USA. [4]Stevens Neuroimaging and Informatics Institute, University of Southern California, Los Angeles, CA 90033, USA. [5]Department of Bioengineering, University of California Riverside, Riverside, CA 92521, USA. [6]Rancho Los Amigos National Rehabilitation Center, Downey, CA 90242, USA. [7]T&C Chen Brain-Machine Interface Center, California Institute of Technology, Pasadena, CA 91125, USA. [8]Cherng Department of Medical Engineering, California Institute of Technology, Pasadena, CA 91125, USA. [9]Howard Hughes Medical Institute, Pasadena, CA 91125, USA.
*Corresponding author. Email: sumnern@caltech.edu (S.L.N.); cliu@usc.edu (C.L.); richard.andersen@vis.caltech.edu (R.A.A.); mikhail@caltech.edu (M.G.S.)
†These authors contributed equally to this work.

signals accurately reflect neuronal firing in both time and space (*4*). As a result, fUSI is a functional brain imaging technique that enables extensive brain coverage recording with single-trial sensitivity in a moving individual. In recent work, we decoded the intentions and goals of nonhuman primates from fUSI data (*12*) and subsequently used fUSI as the basis for an ultrasonic brain-machine interface (*13*).

An important direction of this research is therefore the translation of fUSI-based neuroimaging to brain-machine interface applications for human participants. The skull bone substantially reduces signal sensitivity; as a result, most preclinical applications require a craniotomy (*14*), and the few human fUSI studies conducted have required the skull to be removed or absent. These include intraoperative imaging during neurosurgery (*15*–*17*) and recording through the anterior fontanelle window of newborns (*18*). Hemicraniectomy, or partial skull removal, is commonly performed to reduce pathologically high intracranial pressures, including from traumatic brain injury (TBI), stroke, and subarachnoid hemorrhage (*19*–*21*). After a craniectomy, the skull defect is covered by scalp for several weeks or longer depending on clinical progress before a cranioplasty, or skull reconstruction, to replace the missing skull with one of an assortment of reconstruction materials. These include autologous bone, titanium mesh, porous polyethylene, polyether ether ketone (PEEK), and polymethyl methacrylate (PMMA). Recently, customized cranial implants have grown in popularity thanks to their sterility, strength, and cosmetic appeal (*22*). PMMA-based and PEEK-based cranial implants have already received approval from the US Food and Drug Administration (FDA) (*23*, *24*) and are also transparent to ultrasound or "sonolucent" (*25*–*28*).

In our study, we set out to design a skull replacement window so that we could perform fUSI noninvasively in an awake adult human equipped with an ultrasound-transparent "acoustic window" installed as part of a skull replacement procedure after a decompressive hemicraniectomy. We first examined the suitability of two FDA-approved skull replacement materials (PMMA and titanium mesh) for fUSI using an in vitro cerebrovascular phantom and then compared their signal and contrast properties using an in vivo rat cranial defect model. We then designed a PMMA acoustic window that could be permanently installed in a human patient as part of a skull reconstruction. Through this PMMA window and overlaying intact scalp, we demonstrated recording and decoding of functional brain signals as our human participant performed visuomotor tasks, including playing a video game and strumming a guitar in an ambulatory setting outside the operating room.

RESULTS

PMMA cranial implant allows thickness-dependent blood flow imaging

Brain imaging by fUSI is accomplished by acquiring a series of sequential power Doppler images to measure cerebral blood volume (Fig. 1A). The spatiotemporal changes between these images provide real-time visualization of neural activity by neurovascular coupling. To determine whether fUSI signals could be detected through PMMA material (Fig. 1B), we first constructed an ultrasound phantom with flow channels of increasing depth (14 to 44 mm) designed to mimic blood flow in a human brain (Fig. 2A). The 280-μm-diameter flow channels were designed to model pial arteries that largely control cerebral blood flow (*29*, *30*). This cerebrovascular phantom allowed us to measure the signals underlying fUSI in a controlled environment. We compared five different imaging scenarios: no implant, PMMA implant (1, 2, or 3 mm thick), and titanium mesh implant (Fig. 2, B and C). Synthetic red blood cells were passed through the 280-μm-diameter tubing at three lateral (5, 15, 25 mm) and four axial positions (14, 24, 34, 44 mm) at a constant velocity of 27 mm/s. The cerebrovascular phantom was imaged with a linear ultrasound array transmitting at 7.5 MHz, and the power Doppler intensity signals were recorded (Fig. 2D). The power Doppler signal intensity decreased with increasing PMMA implant thickness and with the titanium mesh (Fig. 2, D and E). The signal-to-noise ratio (SNR) decreased with depth of the imaging plane (Fig. 2F). With increasing depth (34 and 44 mm), the titanium mesh decreased SNR compared with no implant, whereas PMMA was similar or increased relative to control (Fig. 2F). These in vitro results confirmed that power Doppler signal was detectable through different thicknesses of the cranial implant.

Skull replacement window allows fUSI imaging in a rodent model

To test the ability to detect functional brain signals through the different cranial implant materials in vivo, we performed fUSI in four rats after placing each of the five implant types on top of their brains after an acute craniectomy (Fig. 2G), and we used a passive visual simulation task in one rat designed to activate the visual system

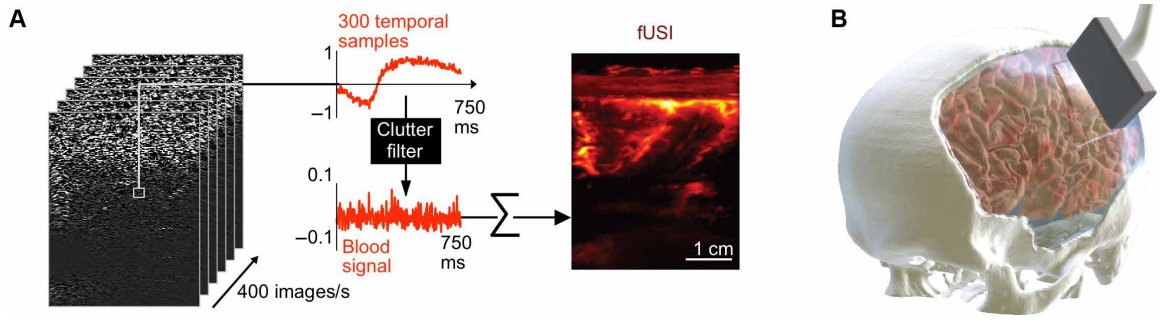

Fig. 1. A custom cranial window enables noninvasive fUSI. (**A**) Schematic of fUSI image collection over time and data processing by clutter filter to exclude tissue motion (left). Two-dimensional reconstructed image of the fUSI recording through the scalp (right). Scale bar, 1 cm. (**B**) Illustration of a human skull reconstructed with a cranial sonolucent window for fUSI with ultrasound probe positioned above window. Image generated using Blender v2.92.

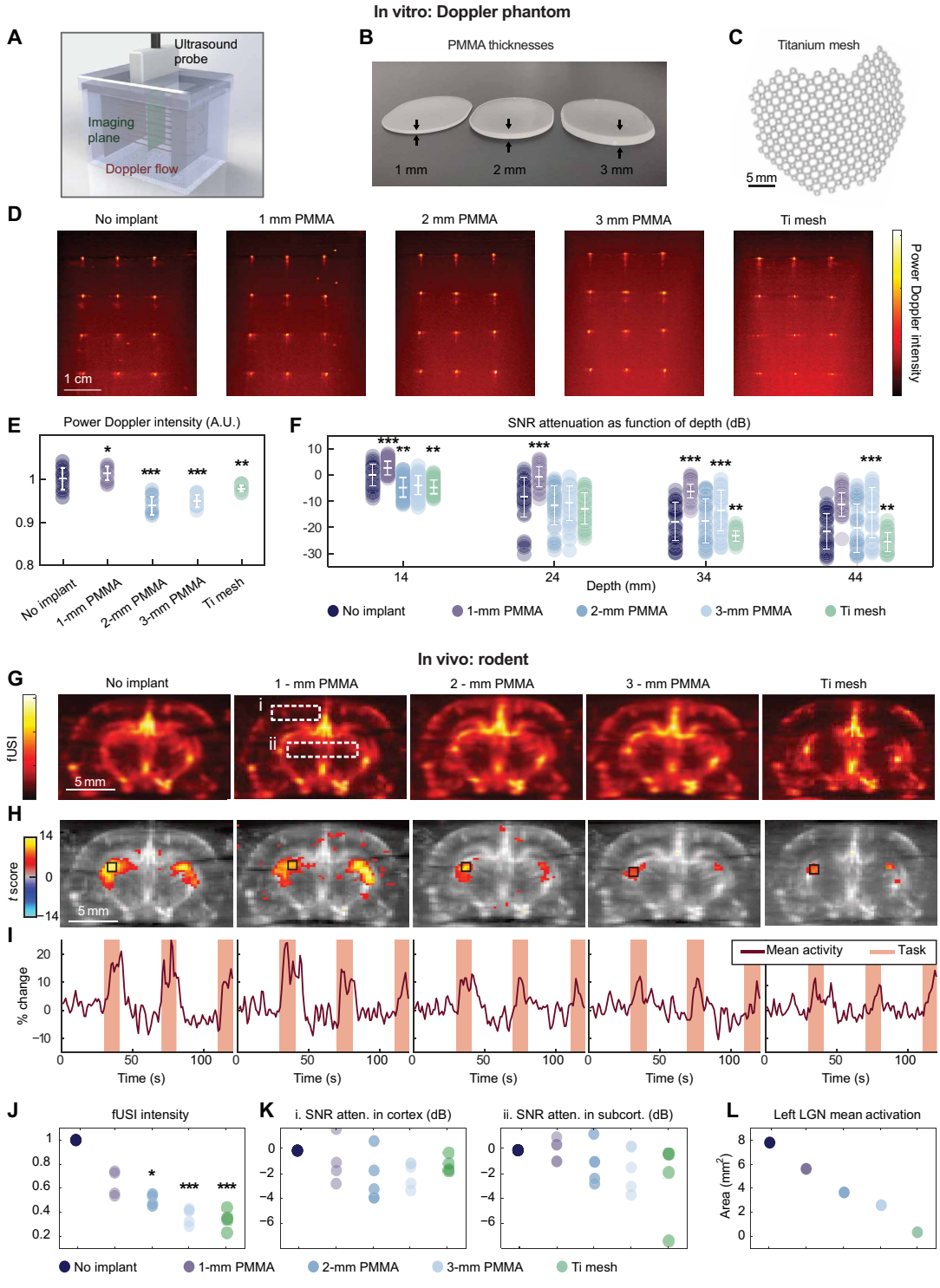

Fig. 2. Polymeric skull replacement materials enable fUSI in a blood flow phantom and in vivo in rat. (**A**) Illustration shows the blood flow phantom. (**B**) Photo of PMMA and (**C**) titanium mesh (Ti mesh) skull implant materials commonly used in cranial reconstruction. (**D**) Power Doppler images of the blood flow phantom with no implant or indicated implant are shown; color scale indicates relative power Doppler signal intensity. Scale bar, 1 cm. (**E**) Power Doppler intensity of blood flow phantom acquired through each implant. Data are presented as mean ± SD; dots represent individual acquisitions, $n = 15$ acquisitions per group. A.U., arbitrary units. (**F**) SNR attenuation for each implant scenario as a function of the depth within the phantom. All values were normalized with the mean value of the no implant control. Data are presented as mean ± SD; dots represent individual acquisitions, $n = 15$ acquisitions per group. (G to J) In vivo imaging through indicated implant material in rat brain. (**G**) fUSI images of the same rat brain with different skull implant materials in the coronal plane: bregma, −3.8 mm. Color scale indicates fUSI signal intensity. Scale bar, 5 mm. Boxes (i) and (ii) correspond to the cortical and subcortical regions studied in (K). (**H**) fUSI with overlaid colors representing change in signal intensity in response to visual stimuli. Color scale, voxels with significant response to visual stimulation ($P_{corrected} < 10^{-5}$) have *T* score overlaid. A GLM was used to calculate the *T* scores and significances. Black box shows the LGN region used to calculate mean fUSI over time (see fig. S2B for enlarged image). Scale bar, 5 mm. (**I**) Time course of power Doppler variation in the LGN region for each skull implant condition in the same rat after visual stimulation is shown. Maroon line represents mean percent change of power Doppler signal in one rat. Orange shading, light-on condition. (**J**) Standardized fUSI intensity ($n = 4$ rats). (**K**) Normalized SNR in cortex (G, i) and in subcortical structures (G, ii) for each skull implant scenario. All values were normalized to the mean value of the no implant control ($n = 4$ rats). (**L**) Significantly activated pixels inside the left LGN in mm^2 after visual stimulation as a function of the implant ($P < 0.05$) ($n = 1$ rat). Data of (E), (F), (J), and (K) were analyzed by one-way ANOVA with post hoc Tukey hsd for comparison between each implant compared with the no implant control (*$P < 0.05$, **$P < 0.01$, and ***$P < 0.001$).

(Fig. 2, H and I). The total fUSI intensity from the whole brain decreased from the no implant scenario by 35% (1 mm PMMA), 50% (2 mm PMMA), 64% (3 mm PMMA), and 66% (titanium mesh) (Fig. 2J). SNR in the cortex [Fig. 2G (i)] decreased slightly with the mesh (−1 dB) and as the PMMA implant thickness increased (−1 dB/mm) [Fig. 2K (i)]. The subcortical structures [Fig. 2G (ii)] within the image showed a similar trend in SNR across the different implant materials [Fig. 2K (ii)]. In all five implant conditions, we identified voxels within the lateral geniculate nucleus (LGN) activated during optical stimulation (Fig. 2, H and I); however, the thicker the implant, the fewer voxels showed significant activation within the LGN, with the least detected activation measured through the titanium mesh [$P < 10^{-3}$, one-way analysis of variance (ANOVA) with post hoc Tukey's honestly significant difference (hsd)] (Fig. 2L). The in vitro cerebrovascular phantom and in vivo results in rodent brains suggested that PMMA was superior to the titanium mesh as an intervening material for fUSI and that making the PMMA window as thin as safely possible would offer the best imaging performance.

Power Doppler images can be acquired through the human scalp before skull reconstruction

To test the possibility of performing fUSI through a chronic cranial window, we recruited a single human participant, an adult male in his thirties. Approximately 30 months before skull reconstruction, the participant suffered a TBI and underwent a left decompressive hemicraniectomy of approximately 16 cm length by 10 cm height (Fig. 1B). Anatomical MRI and fMRI scans were used to map brain structures and functional cortical regions within the borders of the craniectomy (Fig. 3, A and B). Before skull reconstruction with a PMMA implant, the brain of the participant was imaged using power Doppler ultrasound through the intact scalp, with no intervening bone. Power Doppler showed large brain vessels following the curve of sulci folds and smaller vessels irrigating the sulci, which are typical of fUSI images (Fig. 3C). Because of the lack of intracranial pressure and the marked brain motion that results from this condition, we were unable to collect functional data or coregister ultrasound images to anatomical MRIs. Nevertheless, the ability to collect high-quality vascular maps provided evidence that fUSI was possible through an intact human scalp and motivated us to proceed with designing, installing, and testing an acoustic window for the participant.

A customized cranial implant with a 2-mm-thick PMMA window supports functional imaging

To successfully detect functional signal through the customized cranial implant, we collaborated with the attending physician (author C.L.) of the participant and the customized cranial implant manufacturer to design an appropriate acoustic window. In an fMRI study, we identified cortical response fields to a simple finger-tapping task before skull reconstruction (Fig. 3, A and B). fMRI and fUSI both measure neurovascular activity correlated with underlying neural activity (*11*, *14*–*17*). On the basis of the fMRI mapping, a PMMA-customized cranial implant with a 2-mm thickness and a 34 mm–by–50 mm parallelogram-shaped sonolucent "window" was designed and manufactured. The 2-mm-thick portion was positioned above the primary motor cortex, primary somatosensory cortex, and posterior parietal cortex (Fig. 3, D and E). The PMMA implant surrounding the sonolucent window was 4 mm thick. This implant design was calculated by the manufacturer to provide sufficient mechanical performance to serve as a permanent skull replacement.

PMMA acoustic window allows fUSI recording through the skull of a human participant

After skull reconstruction with the acoustic window (Fig. 3, E and F), the brain of the individual was imaged by fUSI (Fig. 3G). The boundaries of the thinned window were located using real-time anatomical B-mode ultrasound imaging, which produces grayscale images of internal body structures. Then a custom-designed cap was used to stably position the ultrasound transducer above the middle of the acoustic 2-mm-thick window. We then manually aligned the fUSI field of view with a previous anatomical MRI, using the known extracranial position and orientation of the ultrasound transducer, along with information about the voxel sizes of both the fUSI and anatomical MRI. The cortical vasculature, including vessels following the curves of sulcal folds and smaller vessels irrigating the adjacent cortex, was observed (Fig. 3G).

On the basis of a prior fUSI recording session and the location of the thinned window, we estimated that the transducer was positioned above the left primary somatosensory cortex (S1) and the supramarginal gyrus (SMG). S1 plays a role in processing somatic sensory signals from the body (*31*, *32*), and the SMG plays a role in grasping and tool use (*33*–*37*); thus, to detect functional brain signals, we instructed the participant to perform two visuomotor tasks (Fig. 4A). The participant was seated in a comfortable chair and facing a screen. In the first task, we used a block design with 100-s rest blocks and 50-s task blocks. During the rest blocks and to minimize extraneous activation, the participant was instructed to close his eyes and relax. During the task blocks, the participant used a video game controller joystick to complete a "connect-the-dots" puzzle on the computer monitor (Fig. 4B). The right thumb was used to move the game controller thumb stick to change the cursor location, whereas the left index finger was used to control the game controller's left shoulder button for a mouse click. The same drawing tasks were repeated across three runs with rest in between. The data from two runs were concatenated and analyzed using a general linear model (GLM) to identify voxels with functional activation. The GLM revealed several brain regions that were or were not task modulated (Fig. 4, C and D). In an unactivated region of interest (ROI) 1, the signal remained stable throughout the run with no significant changes during the task periods ($P > 0.05$, two-sided Student's t test). ROI 1 had an average difference of −0.034% between the drawing and rest blocks ($P = 0.67$, two-sided t test). The active regions identified by GLM displayed positive modulation by the task, demonstrated by increased activity during the drawing blocks and decreased activity during the rest blocks (ROI 2). For example, ROI 2 had an average of 3.68% difference between the drawing and rest blocks ($P < 10^{-10}$, two-sided Student's t test). Although we observed the expected signal according to the expected response of the brain at this recorded location, this study was not designed to reveal whether injury affected the imaging results.

To better understand which voxels in the image contained the most information discriminating the task blocks, we performed a searchlight analysis with a 600-μm radius (Fig. 4E). This searchlight analysis moved a circular window (600-μm radius) across the entire field of view and assessed how well the task information could be decoded with just the voxels contained within that particular

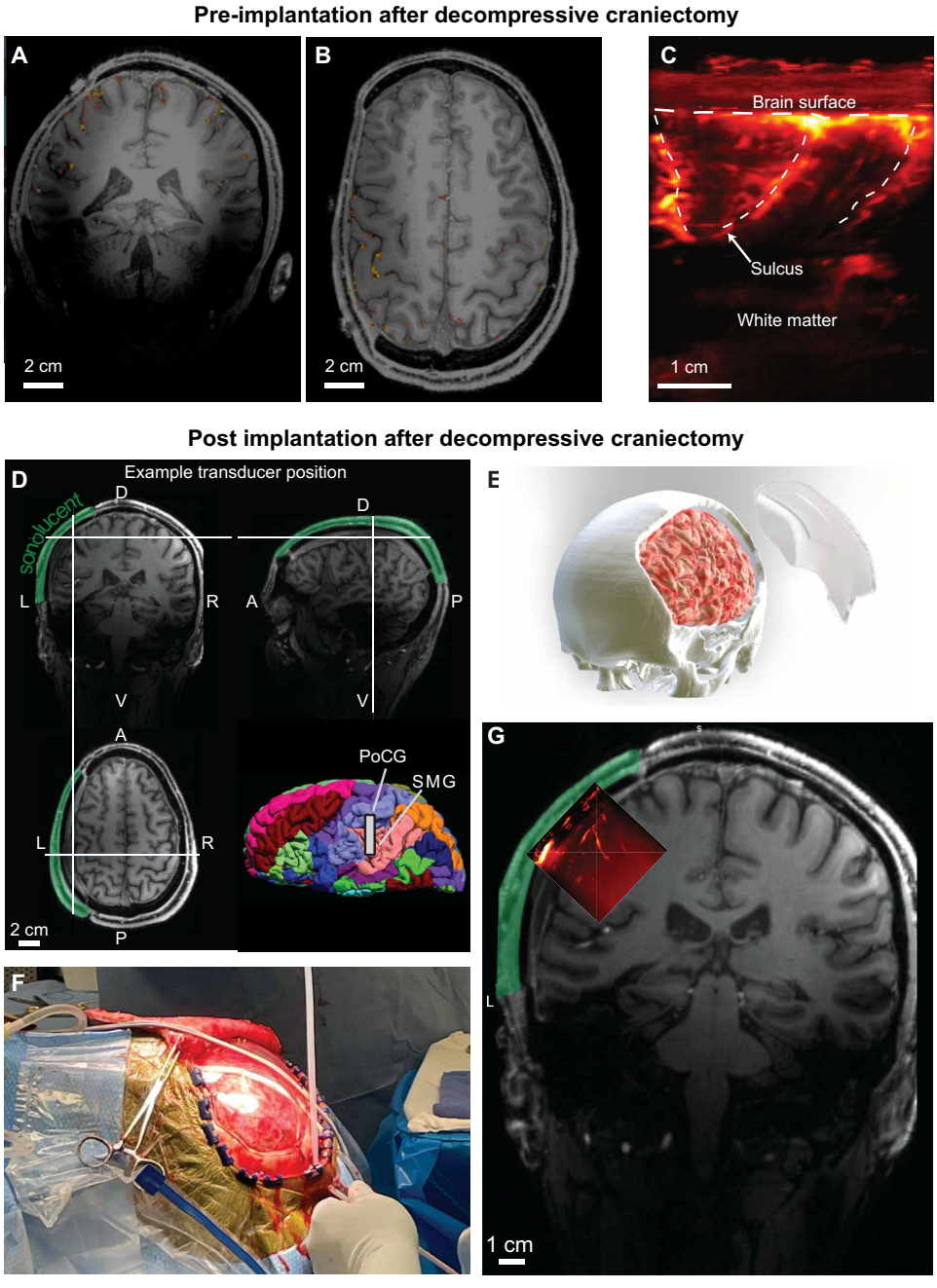

Fig. 3. fUSI enables vascular imaging through intact scalp after decompressive craniectomy and reconstruction with a custom-designed PMMA cranial implant. (**A** and **B**) Brain imaging by fMRI after decompressive hemicraniectomy and before implantation of PMMA cranial implant. Coronal plane (**A**) and transverse plane (**B**) fMRI scan and regions activated during finger-tapping task highlighted in orange. Scale bar, 2 cm. (**C**) Power Doppler image of the participant's brain through the scalp. Scale bar, 1 cm. (**D**) MRI scan of the participant after skull reconstruction with PMMA implant. The white crosses indicate the middle of the transducer during the example fUSI session. Green shading indicates the sonolucent portion of the head including scalp, customized cranial implant, and meninges above the brain. White bar in brain schematic (bottom right) is the estimated position of the transducer. PoCG, postcentral gyrus; D, dorsal; V, ventral, A, anterior; P, posterior, L, left; R, right. Scale bar, 2 cm. (**E**) Diagram of the 4-mm-thick cranial implant with the 2-mm-thick parallelogram-shaped sonolucent window placed above the primary motor, primary somatosensory, and posterior parietal cortex of the adult participant. Image generated using Blender v2.92. (**F**) Reconstruction surgery of the participant with the PMMA custom cranial implant. (**G**) Coregistration of the fUSI imaging plane with an anatomical MR image. Scale bar, 1 cm.

window. This analysis showed that the 5% most informative voxels were distributed across the image and closely matched the results of the statistical parametric map from the GLM. As a very first step toward human brain-machine interface applications, we tested the ability to decode task state (rest versus connect the dots) from single trials of the fUSI data using a linear decoder. We used leave-one-out cross-validation to avoid training the decoder on the same data that was being predicted. We successfully decoded the task state with 84.7% accuracy ($P < 10^{-15}$, one-sided binomial test). When we examined the decoder accuracy across our example session, our linear decoder predicted both the draw and rest blocks with similarly high accuracy (Fig. 4F), with most of the errors occurring at the transitions between the two task states. This effect is likely due in part to the latency between the neural activity and resulting hemodynamic response (*3*, *4*).

In a second task, we asked the participant to play guitar while we recorded fUSI data (Fig. 5A). During the rest blocks (100 s), we instructed the participant to minimize finger or hand movements, close their eyes, and relax. During the task blocks (50 s), the participant played improvised or memorized music on a guitar with right-handed strumming and left fingers moving on the fretboard (Fig. 5B). Using a GLM analysis, several task-activated brain regions were identified, some of which overlapped with those activated during the connect-the-dots task. Statistical analysis revealed significant

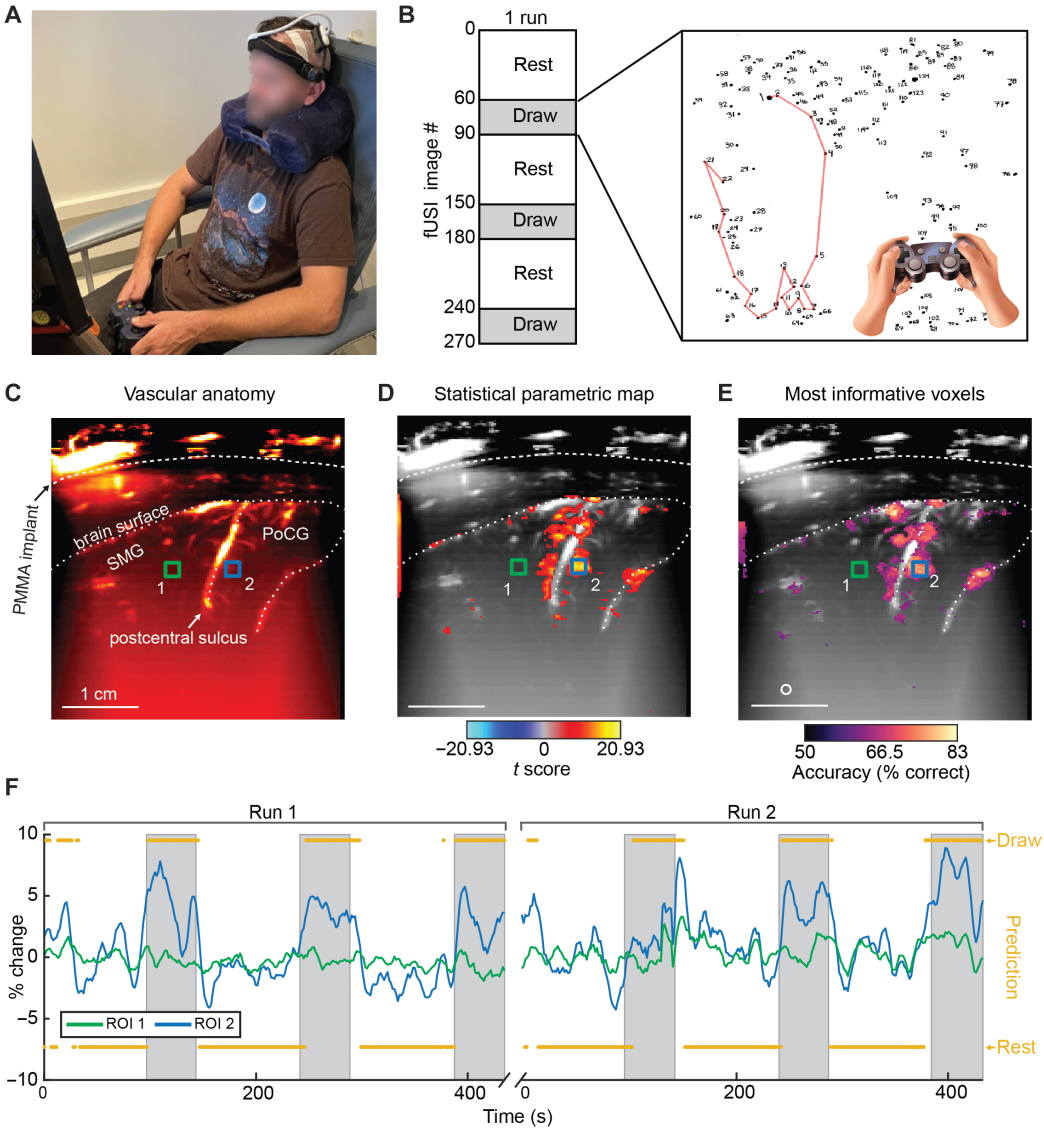

Fig. 4. PMMA cranial window allows noninvasive fUSI imaging and decoding during a video gaming task. (**A**) Representative photograph of participant during video game connect-the-dots task with a joystick during fUSI recording. (**B**) Timeline of rest and draw blocks. In the rest blocks, the participant relaxed and tried to keep a clear mind. In the task blocks, the participant used a game controller to draw lines in a connect-the-dots task. (**C**) Power Doppler images of the vascular anatomy of the imaging plane. Dashed lines highlight specific anatomic features as labeled, including PMMA implant surface, brain surface, and sulcal vessels. Colored boxes show ROIs used in (D) to (F). Scale bar, 1 cm. (**D**) Task-modulated areas across two concatenated runs. Color scale is *T* score statistical parametric map; values are shown for voxels where $P_{corrected} < 10^{-10}$. Scale bar, 1 cm. (**E**) Searchlight analysis showing which small subsets of image voxels contain the most task information. The top 5% of searchlight windows with the highest decoding accuracy superimposed, $P_{corrected} < 2.8 \times 10^{-4}$. White circle, 600-μm searchlight radius. Scale bar, 1 cm. (**F**) Percent change of mean scaled fUSI signal from ROIs. White regions are rest blocks, gray regions are task blocks. Orange annotations show "draw" or "rest" prediction from the linear decoder.

($P < 10^{-10}$, two-sided Student's *t* test) mean differences and *t* scores across three ROIs, indicating task-related neural activity changes. Specifically, ROI 1 and ROI 3 showed substantial mean differences (3.369 and 4.215%, respectively) and high *t* scores (19.661 and 19.886, respectively), with *P* values indicating significance (10^{-10}, two-sided Student's *t* test), whereas ROI 2 exhibited a smaller mean difference (0.254%) and a significant *P* value ($P = 0.003$) (Fig. 5, C and D). Because of the limited amount of data collected during the guitar-playing task, we could not perform a decoding or searchlight analysis.

DISCUSSION

fUSI presents a host of benefits, including increased sensitivity, resolution, and portability, relative to more established techniques such as fMRI (fig. S1). However, fUSI cannot penetrate the adult human skull bone and maintain sufficient sensitivity. In this study, we established the feasibility of fUSI imaging in an awake individual in a nonsurgical setting through a polymeric acoustic window. Before testing this approach in humans, we characterized the acoustic performance of the reconstruction material in vitro and in vivo (rodent) to determine the feasibility of noninvasive imaging through a

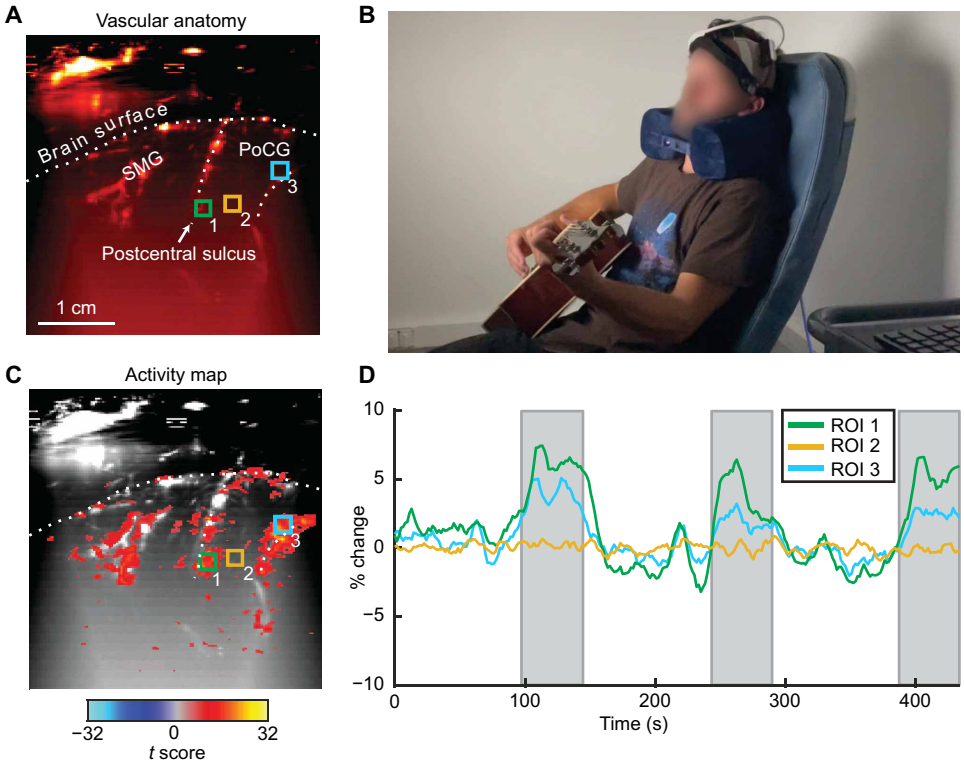

Fig. 5. PMMA cranial implant allows fUSI detection of brain activity during guitar playing. (**A**) Power Doppler image showing the vascular anatomy of the imaging plane. Scale bar, 1 cm. (**B**) Photograph of the participant playing guitar during fUSI recording. (**C**) *T* score statistical parametric map of activity in the guitar-playing task with threshold of $P_{corrected} < 10^{-10}$. Colored boxes 1 to 3 show ROIs used in (D). (**D**) Percent change in mean scaled fUSI signal from ROIs during guitar-playing task. White regions are rest blocks; gray regions are task blocks.

customized cranial implant and to design an appropriate acoustic window. We subsequently acquired noninvasive fUSI recordings of functional brain activity in an awake adult participant undertaking two tasks outside of a surgery environment. We additionally demonstrated decoding of task-associated human brain states for specific activities. Our success in using fUSI to decode brain states serves as a precursor to ultrasonic brain-machine interfaces in humans. Furthermore, our overall approach opens potential applications in both research and clinical use.

Monitoring anatomical and functional brain recovery after a cranioplasty is currently difficult and expensive. Behavioral assessments, such as cognitive status examination, mini-mental state examination, or functional independence measure are commonly used to assess neuropsychological recovery after TBIs (*38*–*40*) but cannot identify specific sites of damage or track recovery at these anatomical locations. Less commonly, computed tomography (CT) and MRI are used to assess anatomical and functional recovery (*41*). However, these methods have low sensitivity and specificity for assessing brain recovery, are expensive (CT and MRI), and can add risk to the patient (CT). In the future, fUSI and custom cranial implants with acoustic windows may enable routine monitoring during the postoperative period for both anatomical and functional recovery. In addition to generalized postoperative monitoring, some patients with TBI will develop specific pathologies that would benefit from increased monitoring frequency. For example, syndrome of the trephined (SoT) is an indication where patients develop neurological symptoms, such as headaches, dizziness, and cognitive impairments, because of altered cerebrospinal fluid dynamics and changes in intracranial pressure after a large craniectomy (*42*). Recording brain activity from these patients with TBI sequelae or SoT may provide insight into the pathophysiology of their disease processes and subsequent recovery.

An additional example of how to assess TBI sequelae or SoT might be through experiments that assess functional connectivity or the similarity between brain signals from two or more areas. Functional connectivity is believed to reflect the existence of direct neuroanatomical connections, and neurological injuries can affect functional connectivity (*43*). The human fUSI methods demonstrated here could be extended to record resting-state activity from multiple brain regions simultaneously and assess changes in functional connectivity across many months as signs of recovery from TBI or as a way to detect early signs of SoT.

One of the most important bottlenecks to human neuroscience research and the development of less invasive brain-machine interfaces is the limited access to human patients for obtaining neural activity data. The ability to measure fUSI signals from ambulatory adult humans with a fully reconstructed skull has the potential to address this challenge, opening opportunities for advancements in these research areas. Approximately 1.7 million people suffer from a severe TBI each year in the United States (*44*). If only a small fraction of these patients receives a cranial implant with an acoustic window as part of their standard of care, it would provide a major opportunity to measure mesoscopic neural activity with excellent spatiotemporal resolution and high sensitivity in humans. In those patients with minimal long-term neurological damage, it will also enable new investigations into advanced neuroimaging techniques and brain-machine interfaces. As we demonstrated in this paper, fUSI has high sensitivity to detect task-modulated brain signals even through the acoustic window. Not only could we identify task-modulated areas by averaging across all task blocks and using a

GLM, but we could also use a linear decoder to robustly decode the current task block using single fUSI images. In the future, we envision this cranial window may enable fUSI of freely walking human participants. Although our human recordings have been entirely done through a PMMA skull implant, we hypothesize that alternative ultrasound-transparent (*26*) materials may also be usable, such as PEEK.

Other human brain imaging modalities exist, including fMRI, diffuse optical tomography (DOT), and fNIRS. These methods have various trade-offs compared with fUSI. fUSI has approximately 10 times the sensitivity of fMRI (*13*), is more portable, and is less restrictive than an MRI bore opening. However, fMRI can obtain whole-brain images. There is currently work on expanding the field of view of volumetric fUSI, but the current best is 80 mm by 20 mm by 40 mm (*17*). For now, one solution for this limitation of fUSI would be using fMRI to identify areas of interest from the entire brain and then using fUSI to precisely track the functional information within one or more of these areas of interest. DOT uses near infrared to infer optical properties of the illuminated tissue and can be used to noninvasively image the brain. This method has several advantages over fUSI, including being able to image through intact skull and having a large field of view. However, it also has several downsides, including needing to solve an ill-posed nonlinear inverse scattering problem, having low spatial resolution (>1 cm), and being limited to approximately 1 cm in depth (*45*). In this study, we used a 7.5-MHz transducer to balance spatial resolution (200 μm) and imaging depth (3 to 5 cm). If imaging deeper brain regions becomes more important, lower-frequency transducers can be used. A 3-MHz transducer, for example, would still have <1 mm spatial resolution and would provide improved sensitivity in deep subcortical areas. fNIRS is an optical technique that uses near-infrared spectroscopy to measure concentrations of deoxygenated and oxygenated hemoglobin. Similar to the disadvantages of DOT, fNIRS has worse spatial resolution (around 2 cm) and brain penetration (1 to 2 cm) compared with fUSI. However, in its favor, fNIRS is a portable technique and allows individuals to freely move about and interact with their environment (*46*). Currently fUSI requires a large cart to hold the ultrafast ultrasound acquisition system, although there is work on miniaturizing the required equipment.

Our study is not without limitations. The approach presented in this study relies on implantation of a cranial window in the skull. Although such an implant could be considered minimally invasive in the context of a patient already undergoing cranioplasty, the requirement for its surgical installation will limit the population of patients for whom this approach is appropriate. Moreover, the portability of the resulting brain interface is impeded by the current need to connect the ultrasound probe to a scanner, which in turn necessitates an electrical outlet. This lack of portability will hinder behavioral applications that rely on freedom from cable connections. Furthermore, the imaging field of view demonstrated in this study is limited to two-dimensional planes covering a relatively small brain volume. These technical limitations underscore the need for hardware advancements to enable untethered, volumetric, large-scale functional imaging. Although this study has demonstrated the capability of fUSI to detect brain activation resulting from multiple tasks, such as video gaming and guitar playing, future work is needed to uncover and decode more precise connections between the observed brain activity and specific task stimuli and behaviors. For example, we identified areas of the brain modulated during the guitar-playing blocks, but it remains unknown specifically what component of the guitar playing modulated the observed neurovascular activity, such as somatosensation, auditory percepts, or motor movements to play the guitar. Last, although our demonstration of successful imaging in a human participant provides an essential proof of concept, future investigations are needed to generalize our findings to larger and more diverse cohorts.

Our results suggest that acoustic windows for fUSI could bridge the gap between existing high-precision but highly invasive neural recording and noninvasive but lower-precision technologies for neural recording. The 38 mm–by–50 mm field of view, high spatial precision (200 μm), and high sensitivity (single-trial decoding) demonstrated by this technology provided access to brain activity in an adult human with a fully reconstructed skull. This access has the potential to directly benefit patients with a brain injury and open new doors to neuroscience discoveries and the development of improved treatments and brain-machine interfaces.

MATERIALS AND METHODS

Study design

The objective of this study was to evaluate the feasibility of fUSI in an awake adult participant equipped with an ultrasound-transparent acoustic window installed during skull replacement after decompressive hemicraniectomy. We first assessed the suitability of FDA-approved skull replacement materials for fUSI using in vitro and in vivo models. We designed an ultrasound phantom with flow channels mimicking blood flow in a human brain, comparing imaging scenarios with different thicknesses of PMMA implants and a titanium mesh implant. In vitro acquisitions were performed with at least 15 temporal power Doppler replicates per condition to ensure robustness and reliability of the data. In vivo fUSI experiments were conducted in four rats (Caltech Institutional Animal Care and Use Committee protocol number IA22-1729). Signal and contrast properties of various implant materials were compared in each animal; the order of the cranial implant materials was randomized in each animal. Visual activation recording was conducted in a single rat. No statistical tests were used to predetermine sample sizes, but our sample sizes were similar to those reported in previous publications (*5*, *14*). For the human study, all procedures were approved by the Institutional Review Boards of the University of Southern California (USC), Caltech (IR19-0902), and Rancho Los Amigos National Rehabilitation Hospital (RLA). We recruited and obtained consent from a 35-year-old male participant with TBI. The participant underwent MRI and fUSI imaging before and after he was fitted with the custom cranial implant with as many acquisitions as allowed by the authorized protocol. During the fUSI recording, the participant engaged in two activities: playing a video game and playing the guitar.

Implant materials

PMMA implants of thicknesses ranging from 1 to 3 mm were supplied by Longeviti Neuro Solutions LLC. Flat PMMA implants (Fig. 2B) were used for the in vitro and rodent study, and a customized PMMA was tailored to the skull shape of the patient. Titanium mesh implants, featuring pure titanium and a thickness of 0.6 mm, with honeycomb patterns alternating between small circles (1.5 mm diameter) and large circles (3 mm diameter), were purchased from KLS Martin.

Functional ultrasound imaging

fUSI visualizes neural activity by mapping local changes in cerebral blood volume, which are tightly linked to neuronal activity through the neurovascular coupling (*47*) and are evaluated by calculated power Doppler variations in the brain (*6*). fUSI used an ultrasonic probe centered at 7.5 MHz (bandwidth >60%, 128 elements, and 0.300-mm pitch, Vermon) connected to a Verasonics Vantage ultrasound system (Verasonics Inc.) controlled by custom MATLAB (MathWorks) B-mode and fUSI acquisition scripts. Each power Doppler image was obtained from the accumulation of 300 compounded frames acquired at a 400-Hz frame rate. Each compounded frame was created using two accumulations of five tilted plane waves (−6°, −3°, 0°, 3°, and 6°). We used a pulse repetition frequency of 4000 Hz. fUSI images were repeated every 1.65 s. Each block of 300 images was processed using a singular vector decomposition (SVD) clutter filter (*33*) (SVD threshold = 50 for rat recording and SVD threshold = 40 for human recording) to separate tissue signal from blood signal to obtain a final power Doppler image exhibiting artificial (for in vitro experiment) or cerebral blood volume in the whole imaging plane (Fig. 1E).

In vitro tissue anatomical and Doppler phantoms

We routed 280-μm-inner-diameter polyethylene tubing through a hollow, box-shaped, 3D-printed, nylon cast at three lateral positions and five axial positions (15 grid points, total). We then created a gelatin phantom using 5% unflavored gelatin, 1% graphite powder, and 5% isopropyl alcohol, to mimic the scattering effects of biological soft tissue (*48*). The gelatin was dissolved in water at low temperatures and then heated to fully dissolve the gelatin before adding the remaining ingredients. After mixing, the solution was cooled to 27°C, poured into a mold, and chilled to maintain its consistency. Once the phantom cast had set and solidified, we flowed a red blood cell phantom liquid (CAE Blue Phantom Doppler Fluid) through the tubing using a peristaltic pump and a long recirculating route with a low pass filter to create a smooth flow at velocities of approximately 0.1 ml min^{-1}. All values were normalized with the mean value of the no-implant case.

In vivo fUSI comparative study in rat

Four Long-Evans rats were used in this study (15 to 20 weeks old, 500 to 650 g, Caltech protocol number IA22-1729). During the surgery and the subsequent imaging session, the animals were anesthetized using an initial intraperitoneal injection of xylazine (10 mg/kg) and ketamine (Imalgene, 80 mg/kg). The scalp of the animals was removed, and the skull was cleaned with saline. A craniectomy was performed to remove 0.5 mm by 1 cm of the skull by drilling (Foredom) at low speed using a microdrill steel burr (burr number 19007-07, Fine Science Tools). We took care to avoid damage to the dura and prevent brain inflammation. After surgery, the surface of the brain was rinsed with sterile saline, and ultrasound coupling gel was placed on the window. The linear ultrasound transducer was positioned directly above the cranial window at coordinate bregma −3.8 mm (coronal plane), and a fUSI scan was performed. We then placed the 1-, 2-, and 3-mm- thick PMMA materials or the titanium mesh above the brain and repeated the fUSI acquisition. To minimize any effect of visual desensitization, we randomized the order of the cranial implant materials in each animal. To quantitatively characterize the fUSI sensitivity through the different PMMA thicknesses, we calculated blood vessels SNR in the cortex and in deeper thalamic regions from the same animal with different implants. Two ROIs were selected for each implant condition (i, cortex; and ii, subcortical regions) (fig. S2A). For each horizontal line of these ROIs, the lateral intensity was plotted, and local maxima (blood vessels) and minima were identified (fig. S2, B and C). SNR was then calculated as $SNR = \frac{mean\ (local\ maxima)}{mean\ (local\ minima)}$.

All values were normalized with the mean value of the no implant case. Differences between standardized SNR for no implant and each skull implant scenario did not show statistical differences ($P > 0.05$). fUSI with visual stimuli was performed in one animal. Visual stimuli were delivered using a blue light-emitting diode (LED; 450-nm wavelength) positioned at 5 cm in front of the head of the rat. Stimulation runs consisted of periodic flickering of the blue LED (flickering rate, 5 Hz) using the following parameters: 50 s of dark followed by 16.5 s of light flickering, repeated three times for a total duration of 180 s. The percentage of change of power Doppler signal in the ROI (Fig. 2H) is plotted for each condition (Fig. 2I). At this distance, the light luminance was 14 lux when the light was on and 0.01 lux when the light was off.

fUSI data processing

For the rodent and human in vivo experiments, we used a GLM to find which voxels were modulated by the visual task. To perform this GLM, we first preprocessed the fUSI data with rigid body motion correction (*49*), followed by spatial smoothing [2D Gaussian with σ = 1 (full-width half max = 471 μm)] and a voxel-wise moving average temporal filter (rat, two time points; and human, five time points). We then scaled the fUSI signal by its voxel-wise mean so that all the runs and voxels had a similar signal range (*50*). To generate the GLM regressor for the visual task, we convolved the block task design with a single gamma hemodynamic response function (HRF) (*51*). For the rodent experiments, the HRF time constant was (τ) = 0.7, time delay (δ) = 1 s, and phase delay (n) = 3 s. For the human experiments, the values were τ = 0.7, δ = 3 s, and n = 3 s. We next fit the GLM using the convolved regressor and the scaled fUSI signal from each voxel. We determined statistical significance of the β coefficients for each voxel using a T contrast with false discovery rate (FDR) correction ($P_{corrected} < 10^{-5}$ for rodent experiments and $P_{corrected} < 10^{-3}$ for human experiments). For the voxel-wise GLM and T contrasts comparing activity between rest and activity blocks in both rodent and human experiments, the data distributions were assumed to be normal, but this was not formally tested.

Human participant

We recruited and obtained consent from a 35-year-old male individual (participant J) with a prior TBI to participate in a research study examining the ability to record functional ultrasound signals through a custom cranial implant. All procedures were approved by the Institutional Review Boards of the USC, California Institute of Technology (Caltech), and RLA. Caltech reference number IR19-0902. All fUSI study sessions took place at Caltech. All CT and MRI scans occurred at the Keck Hospital of USC.

Decompressive hemicraniectomy and reconstruction procedure

The participant underwent a decompressive hemicraniectomy after a severe TBI on 9 April 2019. The approximate size of the craniectomy was 16 cm in anterior-posterior by 10 cm dorsal-ventral (Fig. 3B). A 700-μm isotropic anatomical MRI was acquired shortly

after the hemicraniectomy, and a fUSI scan through the cranial window was acquired at the beginning of September 2021. The participant underwent a left cranioplasty using the Longeviti ClearFit custom skull implant on 22 September 2021. The surgery was performed at Rancho Los Amigos National Rehabilitation Center. The surgery was completed in the standard fashion. In brief, after general anesthesia was induced, the left side of the head was prepped and draped. The prior hemicraniectomy incision was opened, the scalp was dissected from the dura, and the edges of the skull defect were identified circumferentially. An epidural surgical drain was placed, and the cranioplasty implant was secured to the skull using titanium microplates and screws before the wound was closed in multiple layers. As with any intracranial procedure, there is risk of bleeding, CSF leak, or dural puncture. A surgical drain was placed to minimize the accumulation of epidural fluid and was removed after 3 days.

Skull implant design

The PMMA skull implant (Longeviti ClearFit) was designed to fit the hemicraniectomy and match the geometry of the right side of the intact skull. The implant was 4 mm thick to match the participant's nominal bone thickness except for a 34 mm–by–50 mm parallelogram-shaped window of 2-mm-thick PMMA positioned over the area of the brain known to be active during finger tapping, on the basis of the results of an fMRI experiment (Fig. 3, A and B).

Human fMRI task

The participant underwent an fMRI scan during which he performed a finger-tapping task with a block design of 30-s rest followed by 30-s sequential finger tapping with his right hand (Fig. 3A). These blocks were repeated seven times for a total scan duration of 8 min. Instructions for start and end of finger-tapping epochs were delivered with auditory commands delivered through MR compatible headphones. The fMRI acquisition was done on a 7-T Siemens Magnetom Terra system with a 32-channel receive 1Tx head coil with a multiband gradient echo planar imaging T2*-weighted sequence with 1-mm^3 isotropic resolution, 192 mm–by–192 mm field of view, 92 axial slices, repetition time (TR) of 3000 ms, echo time (TE) of 22 ms, 160 volumes, flip angle (FA) of 80°, anterior-posterior phase encoding direction, integrated parallel imaging techniques (iPAT) of 3, and simultaneous multi-slice (SMS) of 2. An anatomical scan was also acquired using a T1-weighted MPRAGE sequence with 0.7-mm^3 isotropic resolution, 224 mm–by–224 mm field of view, 240 sagittal slices, TR/TE of 2200 ms/2.95 ms, and FA of 7°. Statistical analysis of fMRI data was performed with a GLM using Statistical Parametric Mapping (SPM12) (*51*). Preprocessing included motion-realignment, linear drift removal, and coregistration of fMRI data to a high-resolution anatomical scan.

Human fUSI tasks

Ten to 12 months after skull reconstruction, participant J underwent fUSI scans. The participant was seated in a reclining chair with a 27-inch fronto-parallel screen (Acer XB271HU) positioned 70 cm in front of him. The participant controlled the behavioral task using a Logitech F310 Gamepad. We used Gopher (https://github.com/Tylemagne/Gopher360) to enable control of the computer with the Logitech Gamepad. The right thumbstick controlled the position of the computer cursor, whereas the left shoulder button functioned as the left mouse button. We used a block design for the drawing task with 100-s rest blocks followed by 50 s of drawing with the gamepad. We verbally instructed the participant for each rest or task block. The participant was instructed to complete one of multiple connect-the-dots drawings (Fig. 4B). When the participant finished one of the drawings, we presented a new drawing for him to complete. For the rest blocks, we instructed the participant to rest with closed eyes and relaxed mind. We acquired fUSI data at 0.6 Hz (1.65 s per frame). For the guitar-playing task, we used an identical block design with 60-frame rest blocks followed by 30-frame task blocks. In the task blocks, the participant used the left hand to form chords on the fretboard and the right hand to strum the strings.

Task decoding

To decode whether a given timepoint was in a "task" or "rest" block, we used principal components analysis (PCA) for dimensionality reduction and linear discriminant analysis (LDA) for classification. We first labeled each motion-corrected fUSI time point ("sample") as "rest" or "task." We then balanced the dataset to have an equal number of rest and task time points. We then split the dataset into block pairs (1 block pair = rest + task) to avoid training the classifier on time points immediately adjacent to the test time points. This helped ensure that the model would generalize and that our model was not memorizing local patterns for each block pair. We then applied a 2D Gaussian smoothing filter ($\sigma = 1$) to each sample in the train and test sets. We z-scored the training set across time for each voxel. We then trained and validated the PCA + LDA classifier using a block-wise leave-one-out cross-validator; we trained on five blocks and then tested on the held-out block pair's time points. For the PCA, we kept 95% of the variance. To generate the example session decoding, we trained on five blocks with balanced samples of rest and draw and then tested on the unbalanced final block (60 fUSI frames of rest data and 30 fUSI frames of draw task).

Searchlight analysis

Searchlight analysis was used to identify how much task information different parts of an image or volume contain. It produces information maps by measuring the decoding performance in small windows, or "searchlights," centered on each voxel (*52*). For the searchlight analysis used here, we defined a circular ROI (600-μm radius) and, using only the pixels within the ROI, we performed the task decoding analysis. We assigned that ROI's percent correct metric to the center voxel. We then repeated this across the entire image, such that each image pixel is the center of one ROI. To visualize the results, we overlaid the percent correct metric onto a vascular map and kept the 5% most significant voxels. We only ran the searchlight analysis on brain voxels, ignoring all voxels above the brain surface.

Statistical analysis

All raw, individual-level data for experiments where $n < 20$ are presented in data file S1. Unless otherwise stated, a significant difference was considered $P < 0.01$. Comparisons between two groups were performed using a two-sided Student's t test. Comparisons between more than two groups were performed using one-way ANOVA with Tukey hsd post hoc test. For the decoding analysis, a binomial test was used to assess statistical significance ($P < 10^{-10}$). All statistical analysis was performed in MATLAB 2021b. For the GLM, P values were corrected for multiple testing using the false discovery rate method. For the comparison between SNR of skull implant conditions, P values were corrected for multiple testing using the Bonferroni method.

Supplementary Materials

This PDF file includes:
Figs. S1 and S2
Reference (*54*)

Other Supplementary Material for this manuscript includes the following:
Data file S1
MDAR Reproducibility Checklist

REFERENCES AND NOTES

1. C. Errico, J. Pierre, S. Pezet, Y. Desailly, Z. Lenkei, O. Couture, M. Tanter, Ultrafast ultrasound localization microscopy for deep super-resolution vascular imaging. *Nature* **527**, 499–502 (2015).
2. N. Renaudin, C. Demené, A. Dizeux, N. Ialy-Radio, S. Pezet, M. Tanter, Functional ultrasound localization microscopy reveals brain-wide neurovascular activity on a microscopic scale. *Nat. Methods* **19**, 1004–1012 (2022).
3. J. Claron, M. Provansal, Q. Salardaine, P. Tissier, A. Dizeux, T. Deffieux, S. Picaud, M. Tanter, F. Arcizet, P. Pouget, Co-variations of cerebral blood volume and single neurons discharge during resting state and visual cognitive tasks in non-human primates. *Cell Rep.* **42**, 112369 (2023).
4. A. O. Nunez-Elizalde, M. Krumin, C. B. Reddy, G. Montaldo, A. Urban, K. D. Harris, M. Carandini, Neural correlates of blood flow measured by ultrasound. *Neuron* **110**, 1631–1640.e4 (2022).
5. E. Macé, G. Montaldo, I. Cohen, M. Baulac, M. Fink, M. Tanter, Functional ultrasound imaging of the brain. *Nat. Methods* **8**, 662–664 (2011).
6. T. Deffieux, C. Demene, M. Pernot, M. Tanter, Functional ultrasound neuroimaging: A review of the preclinical and clinical state of the art. *Curr. Opin. Neurobiol.* **50**, 128–135 (2018).
7. C. Rabut, S. Yoo, R. C. Hurt, Z. Jin, H. Li, H. Guo, B. Ling, M. G. Shapiro, Ultrasound technologies for imaging and modulating neural activity. *Neuron* **108**, 93–110 (2020).
8. G. Pinton, J.-F. Aubry, E. Bossy, M. Muller, M. Pernot, M. Tanter, Attenuation, scattering, and absorption of ultrasound in the skull bone. *Med. Phys.* **39**, 299–307 (2012).
9. V. Krishna, F. Sammartino, A. Rezai, A review of the current therapies, challenges, and future directions of transcranial focused ultrasound technology: Advances in diagnosis and treatment. *JAMA Neurol.* **75**, 246–254 (2018).
10. F. T. H. Yu, G. Cloutier, Experimental ultrasound characterization of red blood cell aggregation using the structure factor size estimator. *J. Acoust. Soc. Am.* **122**, 645–656 (2007).
11. D. Boido, R. L. Rungta, B.-F. Osmanski, M. Roche, T. Tsurugizawa, D. L. Bihan, L. Ciobanu, S. Charpak, Mesoscopic and microscopic imaging of sensory responses in the same animal. *Nat. Commun.* **10**, 1–13 (2019).
12. S. L. Norman, D. Maresca, V. N. Christopoulos, W. S. Griggs, C. Demene, M. Tanter, M. G. Shapiro, R. A. Andersen, Single-trial decoding of movement intentions using functional ultrasound neuroimaging. *Neuron* **109**, 1554–1566.e4 (2021).
13. W. S. Griggs, S. L. Norman, T. Deffieux, F. Segura, B.-F. Osmanski, G. Chau, V. Christopoulos, C. Liu, M. Tanter, M. G. Shapiro, R. A. Andersen, Decoding motor plans using a closed-loop ultrasonic brain-machine interface, 2022.11.10.515371 (2022).
14. C. Brunner, M. Grillet, A. Urban, B. Roska, G. Montaldo, E. Macé, Whole-brain functional ultrasound imaging in awake head-fixed mice. *Nat. Protoc.* **16**, 3547–3571 (2021).
15. M. Imbault, D. Chauvet, J.-L. Gennisson, L. Capelle, M. Tanter, Intraoperative functional ultrasound imaging of human brain activity. *Sci. Rep.* **7**, 7304 (2017).
16. S. Soloukey, A. J. P. E. Vincent, D. D. Satoer, F. Mastik, M. Smits, C. M. F. Dirven, C. Strydis, J. G. Bosch, A. F. W. van der Steen, C. I. De Zeeuw, S. K. E. Koekkoek, P. Kruizinga, Functional ultrasound (fUS) during awake brain surgery: The clinical potential of intra-operative functional and vascular brain mapping. *Front. Neurosci.* **13**, (2020).
17. S. Soloukey, E. Collée, L. Verhoef, D. D. Satoer, C. M. F. Dirven, E. M. Bos, J. W. Schouten, B. S. Generowicz, F. Mastik, C. I. De Zeeuw, S. K. E. Koekkoek, A. J. P. E. Vincent, M. Smits, P. Kruizinga, Human brain mapping using co-registered fUS, fMRI and ESM during awake brain surgeries: A proof-of-concept study. *Neuroimage* **283**, 120435 (2023).
18. C. Demene, J. Baranger, M. Bernal, C. Delanoe, S. Auvin, V. Biran, M. Alison, J. Mairesse, E. Harribaud, M. Pernot, M. Tanter, O. Baud, Functional ultrasound imaging of brain activity in human newborns. *Sci. Transl. Med.* **9**, eaah6756 (2017).
19. H. Alvis-Miranda, S. M. Castellar-Leones, L. R. Moscote-Salazar, Decompressive craniectomy and traumatic brain injury: A review. *Bull Emerg Trauma* **1**, 60–68 (2013).
20. E. Güresir, P. Schuss, H. Vatter, A. Raabe, V. Seifert, J. Beck, Decompressive craniectomy in subarachnoid hemorrhage. *Neurosurg. Focus* **26**, E4 (2009).
21. L.-P. Pallesen, K. Barlinn, V. Puetz, Role of decompressive craniectomy in ischemic stroke. *Front. Neurol.* **9**, 1119 (2019).
22. C. Iaccarino, A. G. Kolias, L.-G. Roumy, K. Fountas, A. O. Adeleye, Cranioplasty following decompressive craniectomy. *Front. Neurol.* **10**, 1357 (2020).
23. US Food and Drug Administration, Longeviti Neuro Solutions, LLC, 510(k) FDA premarket submission for Longeviti ClearFit Cranial Implant (2019); https://www.accessdata.fda.gov/cdrh_docs/pdf19/K191210.pdf.
24. US Food and Drug Administration, 510(k) FDA premarket submission for OsteoSymbionics PEEK patient-specific cranial implant (2012); https://www.accessdata.fda.gov/cdrh_docs/pdf12/K121102.pdf.
25. T. Shay, K.-A. Mitchell, M. Belzberg, I. Zelko, S. Mahapatra, J. Qian, L. Mendoza, J. Huang, H. Brem, C. Gordon, Translucent customized cranial implants made of clear polymethylmethacrylate: An early outcome analysis of 55 consecutive cranioplasty cases. *Ann. Plast. Surg.* **85**, e27–e36 (2020).
26. M. Belzberg, N. B. Shalom, E. Yuhanna, A. Manbachi, A. Tekes, J. Huang, H. Brem, C. R. Gordon, Sonolucent cranial implants: Cadaveric study and clinical findings supporting diagnostic and therapeutic transcranioplasty ultrasound. *J. Craniofac. Surg.* **30**, 1456–1461 (2019).
27. M. Belzberg, N. B. Shalom, A. Lu, E. Yuhanna, A. Manbachi, A. Tekes, J. Huang, H. Brem, C. Gordon, Transcranioplasty ultrasound through a sonolucent cranial implant made of polymethyl methacrylate: Phantom study comparing ultrasound, computed tomography, and magnetic resonance imaging. *J. Craniofac. Surg.* **30**, e626–e629 (2019).
28. C. Hadley, R. North, V. Srinivasan, P. Kan, J.-K. Burkhardt, Elective sonolucent cranioplasty for real-time ultrasound monitoring of flow and patency of an extra- to intracranial bypass. *J. Craniofac. Surg.* **31**, 622–624 (2020).
29. Imaging of the pial arterial vasculature of the human brain in vivo using high-resolution 7T time-of-flight angiography. *eLife* **11**, e71186 (2022).
30. H. Girouard, C. Iadecola, Neurovascular coupling in the normal brain and in hypertension, stroke, and Alzheimer disease. *J. Appl. Physiol.* **100**, 328–335 (2006).
31. B. P. Delhaye, K. H. Long, S. J. Bensmaia, in *Comprehensive Physiology*, R. Terjung, Ed. (Wiley, 2018), pp. 1575–1602.
32. W. Penfield, E. Boldrey, Somatic motor and sensory representation in the cerebral cortex of man as studied by electrical stimulation. *Brain* **60**, 389–443 (1937).
33. S. K. Wandelt, S. Kellis, D. A. Bjånes, K. Pejsa, B. Lee, C. Liu, R. A. Andersen, Decoding grasp and speech signals from the cortical grasp circuit in a tetraplegic human. *Neuron* **110**, 1777–1787.e3 (2022).
34. G. A. Orban, F. Caruana, The neural basis of human tool use. *Front. Psychol.* **5**, 310 (2014).
35. J. P. Gallivan, D. A. McLean, K. F. Valyear, J. C. Culham, D. Angelaki, Decoding the neural mechanisms of human tool use. *eLife* **2**, e00425 (2013).
36. F. E. Garcea, L. J. Buxbaum, Gesturing tool use and tool transport actions modulates inferior parietal functional connectivity with the dorsal and ventral object processing pathways. *Hum. Brain Mapp.* **40**, 2867–2883 (2019).
37. S. K. Wandelt, D. A. Bjånes, K. Pejsa, B. Lee, C. Liu, R. A. Andersen, Online internal speech decoding from single neurons in a human participant. *MedRxiv*, 11.02.22281775 (2022).
38. N. A. Nabors, S. R. Millis, M. Rosenthal, Use of the neurobehavioral cognitive status examination (Cognistat) in traumatic brain injury. *J. Head Trauma Rehabil.* **12**, 79–84 (1997).
39. E. de Guise, N. Gosselin, J. LeBlanc, M.-C. Champoux, C. Couturier, J. Lamoureux, J. Dagher, J. Marcoux, M. Maleki, M. Feyz, Clock drawing and mini-mental state examination in patients with traumatic brain injury. *Appl. Neuropsychol.* **18**, 179–190 (2011).
40. K. Smith-Knapp, J. D. Corrigan, J. A. Arnett, Predicting functional independence from neuropsychological tests following traumatic brain injury. *Brain Inj.* **10**, 651–662 (1996).
41. R. S. Scheibel, Functional magnetic resonance imaging of cognitive control following traumatic brain injury. *Front. Neurol.* **8**, 352 (2017).
42. V. Joseph, P. Reilly, Syndrome of the trephined. *J. Neurosurg.* **111**, 650–652 (2009).
43. R. Mohanty, W. A. Sethares, V. A. Nair, V. Prabhakaran, Rethinking measures of functional connectivity via feature extraction. *Sci. Rep.* **10**, 1298 (2020).
44. A. Georges, J. M. Das, *Traumatic Brain Injury* (StatPearls Publishing, 2022); https://www.ncbi.nlm.nih.gov/books/NBK459300/.
45. Y. H. M.d, Y. Yamada, Overview of diffuse optical tomography and its clinical applications. *J. Biomed. Opt.* **21**, 091312 (2016).
46. Functional near-infrared spectroscopy reveals brain activity on the move. *Proc. Natl. Acad. Sci. U.S.A.* **119**, e2208729119 (2022).
47. C. Iadecola, The neurovascular unit coming of age: A journey through neurovascular coupling in health and disease. *Neuron* **96**, 17–42 (2017).
48. T. J. Hall, M. Bilgen, M. F. Insana, T. A. Krouskop, Phantom materials for elastography. *IEEE Trans. Ultrason. Ferroelectr. Freq. Control* **44**, 1355–1365 (1997).
49. E. A. Pnevmatikakis, A. Giovannucci, NoRMCorre: An online algorithm for piecewise rigid motion correction of calcium imaging data. *J. Neurosci. Methods* **291**, 83–94 (2017).
50. G. Chen, P. A. Taylor, R. W. Cox, Is the statistic value all we should care about in neuroimaging? *Neuroimage* **147**, 952–959 (2017).
51. G. M. Boynton, S. A. Engel, G. H. Glover, D. J. Heeger, Linear systems analysis of functional magnetic resonance imaging in human V1. *J. Neurosci.* **16**, 4207–4221 (1996).
52. J. A. Etzel, J. M. Zacks, T. S. Braver, Searchlight analysis: Promise, pitfalls, and potential. *Neuroimage* **78**, 261–269 (2013).

53. W. Griggs, ''wsgriggs2/window-to-the-brain: First stable version of Window to Brain code,'' Zenodo 10.5281/zenodo.10656058 (2024).
54. L. Marshall, ''Your Brain on Imagination: It's a Lot Like Reality,'' *Neuroscience News*, 10 December 2018; https://neurosciencenews.com/imagination-reality-10320/.

Acknowledgments: We thank K. Pejsa for administrative assistance and participant planning. We thank M. Tanter at INSERM (Paris, France) for feedback and support throughout the research process. Last, we thank participant J for his willing participation. **Funding:** This work was supported by NIH R01NS123663 (to R.A.A. and M.G.S.); the T&C Chen Brain-Machine Interface Center (to R.A.A. and M.G.S.); the Boswell Foundation (to R.A.A.), National Eye Institute NEI F30 EY032799 (to W.S.G.); a Josephine de Karman Fellowship (to W.S.G.); UCLA-Caltech Medical Scientist Training Program NIGMS T32 GM008042 (to W.S.G.); a Della Martin Postdoctoral Fellowship (to S.L.N.); Human Frontier Science Program Cross-Disciplinary Fellowship LT000217/2020-C (to C.R.); USC Neurorestoration Center (to C.L.); and the Howard Hughes Medical Institute (to M.G.S.). **Author contributions:** C.R., S.L.N., W.S.G., C.L., R.A.A., and M.G.S. conceptualized the study. C.R. and S.L.N. developed the fUSI sequence. S.L.N. designed the Doppler phantom. C.R. and S.L.N. conducted in vitro experiments, and C.R. performed rodent experiments, including surgeries and ultrasound data acquisitions. C.L. recruited study participants, and C.R., S.L.N., and W.S.G. recorded human fUSI data. C.L. and J.J.R. conducted craniectomy and cranioplasty surgeries. K.J. oversaw structural and functional MR imaging and analysis. W.S.G., S.L.N., and C.R. processed and analyzed ultrasound data. M.G.S., R.A.A., C.L., and V.C. supervised the research. C.R., W.S.G., S.L.N., M.G.S., and R.A.A. drafted the manuscript, which was reviewed and edited by C.R., W.S.G., S.L.N., M.G.S., R.A.A., C.L., and V.C. **Competing interests:** C.R., W.S.G., S.L.N., R.A.A., C.L., and M.G.S. have filed a provisional patent application based on this research, filing no. CIT-9020-P entitled "A method for observing brain states using functional ultrasound imaging and a sonolucent material." The other authors declare that they have no competing interests. **Data and materials availability:** All data associated with this study are available in the paper or the Supplementary Materials. The fUSI time series for the in vitro, rodent, and human data presented here are archived and freely available at CaltechDATA (https://doi.org/10.22002/f3y3k-em558). Code used to collect fUSI data, analyze fUSI time series, and generate the key figures and results is publicly available on GitHub at https://github.com/wsgriggs2/window-to-the-brain, and an archived version is stored on Zenodo at https://zenodo.org/doi/10.5281/zenodo.10645590 (*53*).

Submitted 19 June 2023
Resubmitted 1 December 2023
Accepted 7 May 2024
Published 29 May 2024
10.1126/scitranslmed.adj3143